A&A, 708, A52 (2026)
https://doi.org/10.1051/0004-6361/202558182

Astronomy & Astrophysics

Unveiling blazar candidates within unassociated *Fermi* sources through radio and near-infrared observations

C. I. Martínez[1,2,⋆], L. Donoso[3], L. Zibecchi[4,5], R. K. Saito[6], and D. Minniti[7,8]

[1] Observatorio Astronómico Félix Aguilar, Universidad Nacional de San Juan, Av. Benavidez Oeste, 8175 San Juan, Argentina
[2] Consejo Nacional de Investigaciones Científicas y Técnicas (CONICET), Godoy Cruz 2290 Ciudad Autónoma de Buenos Aires, Argentina
[3] Instituto de Ciencias Astronómicas de la Tierra y el Espacio (CONICET-UNSJ), Av. España, 1512 sur, San Juan, Argentina
[4] Facultad de Ciencias Astronómicas y Geofísicas, Universidad Nacional de La Plata, Paseo del Bosque, B1900FWA La Plata, Buenos Aires, Argentina
[5] Instituto de Astrofísica de La Plata (CONICET-UNLP), Paseo del Bosque, B1900FWA La Plata, Buenos Aires, Argentina
[6] Departamento de Física, Universidade Federal de Santa Catarina, Trindade, 88040-900 Florianópolis, Brazil
[7] Instituto de Astrofísica, Departamento de Física y Astronomía, Facultad de Ciencias Exactas, Universidad Andrés Bello, Av. Fernandez Concha 700, Las Condes, Santiago, Chile
[8] Vatican Observatory, Specola Vaticana, V00120, Vatican City State, Italy

Received 19 November 2025 / Accepted 23 February 2026

ABSTRACT

Context. The *Fermi* Large Area Telescope (LAT) detected 7195 γ-ray sources within the first 12 years of scientific observations, spanning an energy range from 50 MeV to 1 TeV. The fourth source catalog 4FGL-DR4 (*Fermi* Gamma-ray LAT Data Release 4), contains 2423 unassociated γ-ray sources (UGSs). This catalog provides an excellent opportunity to explore the scientific potential of these high-energy targets and to identify their counterparts at different wavelengths.
Aims. We identified blazar candidates as counterparts to UGSs in the Galactic plane through a multiwavelength analysis of near-infrared and radio observations.
Methods. We compiled an initial list of 318 non-extended *Fermi* sources located in the Galactic plane. After filtering the list based on interstellar extinction and the 95% confidence *Fermi* error ellipse, we selected 22 UGS for evaluation. We searched the Very Large Array Sky Survey (VLASS) catalog for sources of continuum radio emission near each target on the sample list. We identified a total of 34 radio sources as potential counterparts to the 22 UGSs within the *Fermi* error ellipses. We confirmed these radio sources as blazar candidates by analyzing their associated near-infrared sources using the color-magnitude diagram (CMD), color-color diagram (CCD), and K_s-band variability from the VISTA Variables in the Via Lactea (VVV) catalog. Additionally, we examined the radio spectral energy distribution (SED) using observations from the Rapid ASKAP Continuum Survey (RACS).
Results. We found evidence for the association of five UGSs: four with blazar candidates and one with an elliptical galaxy. Additionally, we estimated its SED using RACS bands.

Key words. BL Lacertae objects: general – gamma rays: general – radio continuum: general

1. Introduction

Discovering new extragalactic objects helps us to understand the large-scale structure of the Universe, ensuring better comprehension of cosmic origins and evolution, as well as the interactions between them. Since the beginning of the 20th century, the number of extragalactic objects discovered has increased dramatically. However, identifying and classifying these kinds of objects in the Galactic plane has been a significant challenge for scientists due to the presence of crowded star fields, dust and gas clouds, reddening, and other factors. These block the light emitted by distant objects such as radio galaxies, quasars, and blazars, which constitute an overall family of active galactic nuclei (AGNs).

The accretion of matter around a supermassive black hole powers an AGN, making it one of the most luminous and energetic astrophysical sources known. There are actually 51 different terms used to classify AGNs (Padovani et al. 2017), which are defined by a broadband continuum emission that extends over a much wider spectral range than normal galaxies. Blazars are an AGN subclass, which can be further divided into BL Lacertae objects (see Stickel et al. 1991 and references therein) and flat-spectrum radio quasars (FSRQ; see Chen et al. 2009). According to the Unified Model (Urry & Padovani 1995), an FSRQ may transition into a BL Lac when it loses power, which results in a rotationally driven structure. However, this transition has not yet been fully proven.

A blazar can emit over the entire electromagnetic spectrum, with highly variable emissions ranging from radio waves to γ-rays (i.e., Lister et al. 2019; D'Abrusco et al. 2019; Marchesini et al. 2019; Paiano et al. 2020; Ajello et al. 2020). The spectral energy distribution (SED) of a blazar consists of two main types of component: low-energy components ranging from infrared to X-rays, which are produced by the synchrotron emission of relativistic particles that are accelerated in the blazar jet; and high-energy components ranging from mega-electron-volt to tera-electron-volt, which are associated with inverse Compton scattering (Fossati et al. 1998) or hadronic processes (Peirson et al. 2022). This nonthermal emission manifests

⋆ Corresponding author: cmartinez@conicet.gov.ar

as powerful, relativistic jets directed toward Earth, oriented at an angle of a few degrees along the line of sight. Radio continuum emission is also associated with these jets (Blandford & Königl 1979). The correlation between radio and γ-ray emission can be explained by a beaming effect. In this way, Yang et al. (2022) found evidence that γ-ray emission is closely related to radio and optical emission. They also found that γ-ray luminosity is correlated with synchrotron peak luminosity. Massardi et al. (2016) studied a sample of blazar candidates and found that most of them (~89%) have remarkably smooth spectra that can be well described by a double power law over the full range. This finding suggests the presence of a single emitting region. The flat behavior of a blazar spectrum may result from the superposition of emissions from different compact regions that are self-absorbed at different frequencies.

Since 2008, the *Fermi* Large Area Telescope (LAT, Atwood et al. 2009) has been studying the γ-ray regime, which is one of the least understood areas of electromagnetic radiation. It has increased the number of high-energy sources by more than an order of magnitude. The fourth source catalog 4FGL-DR4 (*Fermi* Gamma-ray LAT Data Release 4, Ballet et al. 2023), includes 7195 γ-ray sources, 2423 of which (approximately 34%) are not associated with other wavelengths at lower energies. Ackermann et al. (2012) performed a statistical analysis of the first *Fermi*-LAT catalog, focusing on unassociated γ-ray sources (UGSs). They concluded that most AGNs should be found among unidentified sources, particularly at low Galactic latitudes. In general, γ-ray sources can be classified in two ways: by analyzing statistical differences in the *Fermi*-LAT catalogs using machine learning, or by searching for counterparts emission at other wavelengths (Lefaucheur & Pita 2017). One search method is to analyze infrared emissions (Massaro et al. 2011), radio emissions (Massaro et al. 2013), and X-ray emissions (Paggi et al. 2013); another method is to analyze SEDs (Acero et al. 2013). The fifth edition of the Roma-BZCAT catalog of blazars (Massaro et al. 2015) contains the coordinates and multi-frequency data of 3561 blazar sources; however, only 37 of these objects are located on the Galactic plane.

Pichel et al. (2020) used the four-dimensional color space of the near- and mid-infrared (NIR and MIR) to distinguish blazars from other Galactic and extragalactic sources. They used the VISTA Variables in the Via Lactea (VVV, Minniti et al. 2010) and the Wide-field Infrared Survey Explorer (WISE, Wright et al. 2010) for this analysis. In brief, they found that, for each blazar, there was only one VVV source within the 95% confidence positional uncertainty ellipse of the *Fermi* source. These VVV sources coincide with the Roma-BZCAT blazar's position and show different photometric properties when compared with stellar and extragalactic objects. Massaro et al. (2011, 2012a,b, 2015) and D'Abrusco et al. (2019) agree that blazars are clearly distinct from other extragalactic sources observed in the MIR. Using data from the WISE survey in four bands centered at 3.4, 4.6, 12, and 22 μm, they identified a region covered only by blazars.

Bruzewski et al. (2021) presented a catalog of 7432 radio counterpart candidates for 1119 unassociated γ-ray sources selected from the 4FGL Data Release 2. The authors used the Very Large Array Sky Survey (VLASS, Gordon et al. 2021) to quick-look data and conducted *C*-band (4–8 GHz) observations for a total of 57 hours and 2456 pointings. They proposed a method based on the simultaneous detection of radio sources in three different bands. Using this method, they identified 79 compact sources associated with 74 UGS fields and classified them as flat-spectrum sources (spectral index $\alpha < -0.5$).

Marchesini et al. (2023) conducted a multifrequency study of the blazar WISE J141046.00+740511.2. The researchers combined observations from the *Karl G. Jansky* Very Large Array (JVLA) radio interferometer, the Giant Metrewave Radio Telescope (GMRT), the Gran Telescopio Canarias (GTC), the Gemini Observatory, the William Herschel Telescope, and the Liverpool Observatory, together with *Fermi*-LAT and *Swift* data. They modeled the SED of the source to study the parameters that characterize the radio loudness or weakness of blazars.

Recently, Behiri et al. (2025) discovered a significant correlation between 855-MHz radio emissions and γ-ray luminosity. This finding highlights the important role of relativistic jets. They also found that FSRQs exhibit more efficient high-energy pumping and dominate the bright end of the spectrum in the radio and γ-ray bands. In contrast, BL Lacs exhibit greater variability in their spectral behavior, which reflects their evolutionary differences.

This work aims to identify blazar candidates associated with γ-ray sources detected by the *Fermi*-LAT mission using a multifrequency analysis of infrared and radio spectra. Collecting information from these spectral regions and associating it with different types of blazars (such as the blazar sequence; see Cavaliere & D'Elia 2002) allowed us to study the physical processes inside these objects and their possible relationship with other types of galaxies with active nuclei.

In Sect. 2, we describe the selection of the UGS sample list that contains radio emission sources in the long radius of the error ellipse for the 95% confidence *Fermi* sources. In Sect. 3, we define the methodology used to identify candidate blazars associated with radio sources that could be the origin of UGSs. In Sect. 4, we present the results of the five objects detected. Finally, in Sect. 5 we discuss the main results of our work and draw some conclusions.

2. Sample

To select blazar candidates as the origin of UGSs in the Galactic plane, we searched for *Fermi* sources from the 4FGL-DR4 catalog. Since we planned to use VVV survey data, we defined the search areas as follows: $-10^\circ < l < 10^\circ$ and $-10^\circ < b < 5^\circ$ (bulge), and $-65^\circ < l < -10^\circ$ and $-2^\circ < b < 2^\circ$ (adjacent section of the midplane). A total of 318 UGSs were found, with 193 in the bulge and 125 in the midplane.

Compared to optical wavelengths, observations at near-infrared wavelengths minimize the effects of interstellar extinction. According to the distributions of interstellar extinction and the *Fermi* error ellipse, we selected sources with lower interstellar extinction, $A_{K_s} < 1.2$ mag, and a long-radius error ellipse at the 95% confidence level, $amaj_{95} < 5'$. The extinction cut ($A_{K_s} <$ 1.2 mag) ensures reliable IR/optical detections and minimizes biases introduced by highly reddened regions (see Donoso et al. 2024). The long-radius threshold ($amaj_{95} < 5'$), which is close to the median value ($amaj_{95} = 4.25 \pm 3.04'$), significantly reduces the probability of spurious cross-matches. Together, these criteria yield a sample with sufficient photometric quality for follow-up observations. We used the dust estimations of Schlafly & Finkbeiner (2011) and the K_s-band extinction coefficient of Catelan et al. (2011). This filtering yielded 22 UGSs with no association at other wavelengths.

For the blazar hypothesis, we searched for continuum radio emission sources (hereafter referred to as RSs) as counterparts of γ-ray sources in the *S* band ($2 \le \nu \le 4$ GHz) of the VLASS catalog. The search region is defined as the long radius of the

error ellipse for the 95% confidence *Fermi* sources. We searched for radio continuum sources within this region.

For the VLASS catalog results, we eliminated the RSs with a reliability factor (see Gordon et al. 2021) of Quality_flag = 4 (this means that the flux peak is higher than the flux density $F_{\rm peak} > F_{total}$); Quality_flag = 2 (where the $F_{\rm peak}$ is 5 times lower than the local rms noise); and Quality_flag = 1 (RSs with lobe structures). Also, we applied the duplicate detection factor and only used the Duplicate_flag = 0 or 1, meaning that the Python Blob Detection and Source Finding code (PyBDSF, Mohan & Rafferty 2015) did not find duplicated sources. Finally, the list includes 22 UGSs containing at least one continuum radio source in the VLASS catalog within the search region. In total, there are 34 RSs, which are listed in Table 1.

3. Methodology

3.1. Color-color diagrams

We used the photometry of VVV in the Z, Y, J, H, and K_s passbands to find near-IR counterparts of targets from the sample list. Donoso et al. (2024) applied a method to a sample of UGSs in the Galactic regions using the VVV and WISE surveys to identify blazar candidates as counterparts to *Fermi*-LAT sources. According to the conclusions of Cioni et al. (2011), AGNs with point-like morphologies occupy the A region in the $YJKs$ color-color diagram (CCD), while AGNs with confirmed host galaxies occupy the B region. Objects in the C region are reddened Magellanic sources, and the D region is dominated primarily by stars and low-confidence AGNs. Blazars populate different regions in the CCDs because they are dominated by nonthermal emission in the mid-IR (Pichel et al. 2020). Additionally, Baravalle et al. (2023) defined extragalactic sources in the color-magnitude diagrams (CMDs) using the following color criteria: $0.5 < J-K_s < 2$, $0 < J-H < 1$, and $0 < H-K_s < 2$.

In order to associate the RSs from the VLASS catalog with the NIR sources from the VVV catalog, we must define a search radius around the coordinates of each RS. On the one hand, Roma-BZCAT is the most up-to-date compilation of confirmed blazars. We used this catalog to match with the VLASS catalog to find sources near each object classified as a blazar. Figure 1 shows a histogram of the separation between the blazars in the Roma-BZCAT catalog and the nearby continuum radio sources in the VLASS catalog. The mean value for the 2704 targets classified as blazars is 0.48″.

On the other hand, the VLASS catalog was compiled using the VLA radio interferometer with an angular resolution of ∼2.5″ for the B and BnA configurations. We defined the search radius as the root-sum-square of the separation between blazar and radio source (0.48″), and the JVLA resolution (∼2.5″). This resulted in a search radius of 2.55″. Only NIR sources located within 2.55″ of an RS from the sample list were considered counterparts for analysis. We show in Figs. 2, 3, 4, 5, and 6 the VVV images in the K_s band with the contour levels of radio continuum emission at the S band of theVLASS catalog.

CMDs and CCD are constructed using the VVV passbands[1] YJK_s for selected NIR and other sources in the region. Using the classification criteria from Cioni et al. (2013), and the results obtained by Baravalle et al. (2023), we identified five NIR sources as extragalactic objects that satisfy these criteria and are potential blazar candidates for the UGSs J1745.6-3626, J1814.7-3420, J1816.4-2727, J1817.2-3035, and J1828.2-3252.

[1] The VVV photometry was obtained from http://vsa.roe.ac.uk/.

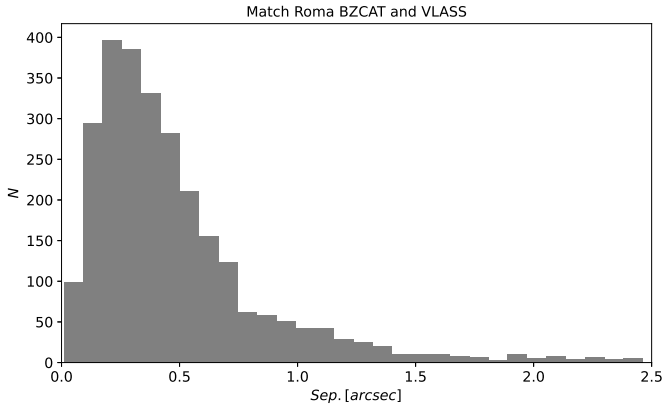

Fig. 1. Histogram of separation between the confirmed blazars in the Roma-BZCAT catalog and the nearby continuum radio source in the VLASS catalog, expressed in arcsec.

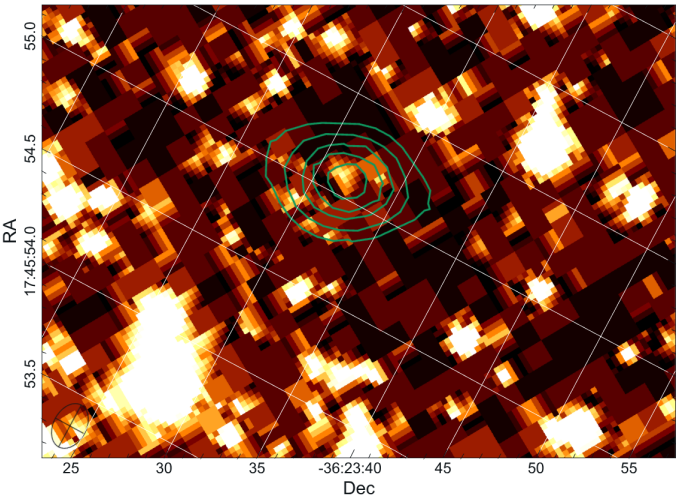

Fig. 2. VVV image in K_s band of RS17 (UGS J1745.6-3626). Green lines show the contour levels of the VLASS J174555.05-362331.3 source.

The CMDs and CCD are shown in Appendix A. For the remaining 16 UGS, there is no NIR source near the radio source that meets the CCD criteria. Table 2 summarizes the NIR sources that could be extragalactic and includes their magnitudes at the Z, Y, J, H, and K_s passbands, as well as their coordinates and separation from the RS.

3.2. Variability

We performed a variability analysis on the K_s-band light curves from the VVV Infrared Astrometric v2 Catalogue (VIRAC2, Smith et al. 2025) for five objects identified in the VVV catalog, which have been suggested as blazar candidates: RS17 (J1745.6-3626), RS23 (J1814.7-3420), RS24 (J1816.4-2727), RS25 (J1817.2-3035), and RS33 (J1828.2-3252). The VIRAC2 is a PSF-based catalog that uses K_s-band epochs from the VVV and VVV eXtended Surveys (Saito et al. 2024), covering a time baseline of approximately 13 years. Using the available photometric data in this band, the corresponding light curves were constructed for each source. Figure 7 plots the K_s magnitude as a function of time for the five blazars candidates. To quantify and assess the significance of the flux variations in our sample, we

Table 1. List of 34 RSs corresponding to 22 UGSs.

4FGL-DR4	VLASS1QLCIR	ID	RA (J2000) [deg]	Dec (J2000) [deg]	$F_{\rm tot}$ [mJy]	σ_S [mJy/beam]	$S_{\rm code}$	Class.
J1714.9-3324	J171442.93-332446.6	RS01	17:14:42.93	–33:24:46.70	29.457 ± 0.299	0.112	S	PN[(a)]
J1731.6-2904	J173141.83-290228.8	RS02	17:31:41.83	–29:02:28.90	1.496 ± 0.344	0.131	C	–
J1733.2-2915	J173318.61-291343.7	RS03	17:33:18.62	–29:13:43.80	3.847 ± 0.285	0.133	S	–
J1734.0-2933	J173405.20-293326.7	RS04	17:34:00.12	–29:30:49.20	1.387 ± 0.336	0.132	S	–
	J173400.11-293049.1	RS05	17:34:05.20	–29:33:26.80	1.104 ± 0.295	0.133	S	–
J1737.2-2421	J173716.38-242127.2	RS06	17:37:16.39	–24:21:27.30	8.003 ± 0.267	0.128	S	–
	J173721.15-242302.9	RS07	17:37:21.15	–24:23:03.00	32.496 ± 1.503	0.126	M	–
J1737.2-2808	J173720.68-281006.7	RS08	17:37:20.68	–28:10:06.80	2.507 ± 0.468	0.138	S	PN[(b)]
	J173710.08-281144.3	RS09	17:37:10.09	–28:11:44.30	1.555 ± 0.261	0.133	S	–
J1737.3-3332	J173724.90-333322.6	RS10	17:37:24.91	–33:33:22.70	3.638 ± 0.526	0.111	S	–
J1739.3-2531	J173928.22-253111.5	RS11	17:39:28.23	–25:31:11.60	2.382 ± 0.350	0.120	S	YSO[(c)]
	J173908.94-253328.4	RS12	17:39:08.95	–25:33:28.40	2.819 ± 0.326	0.125	S	–
J1739.7-2836	J173938.13-283349.4	RS13	17:39:38.14	–28:33:49.50	33.642 ± 1.592	0.146	M	–
	J173937.55-283338.2	RS14	17:39:37.55	–28:33:38.30	24.677 ± 1.836	0.146	M	–
J1745.6-3626	J174527.55-362615.4	RS15	17:45:27.55	–36:26:15.50	10.495 ± 0.308	0.157	M	–
	J174526.72-362612.0	RS16	17:45:26.72	–36:26:12.00	4.911 ± 0.337	0.158	S	–
	J174555.05-362331.3	RS17	17:45:55.06	–36:23:31.30	5.436 ± 0.301	0.159	S	–
J1752.3-3139	J175208.11-313541.8	RS18	17:52:08.11	–31:35:41.90	2.848 ± 0.302	0.150	S	–
J1802.4-3041	J180226.13-304313.7	RS19	18:02:26.13	–30:43:13.70	6.777 ± 0.289	0.115	S	–
J1805.1-3049	J180512.61-304634.6	RS20	18:05:12.61	–30:46:34.60	8.431 ± 0.243	0.118	S	–
J1808.4-3358	J180823.91-335954.2	RS21	18:08:23.91	–33:59:54.28	2.305 ± 0.277	0.112	S	–
J1812.8-3144	J181300.95-314424.3	RS22	18:13:00.96	–31:44:24.40	4.487 ± 0.279	0.118	S	AGN[(d)]
J1814.7-3420	J181446.75-342340.7	RS23	18:14:46.75	–34:23:40.70	1.562 ± 0.209	0.115	S	–
J1816.4-2727	J181628.79-272602.8	RS24	18:16:28.79	–27:26:02.90	3.264 ± 0.227	0.119	S	–
J1817.2-3035	J181720.39-303258.5	RS25	18:17:20.39	–30:32:58.50	5.802 ± 0.221	0.109	S	AGN[(e)]
J1817.9-3334	J181758.82-333235.7	RS26	18:17:58.82	–33:32:35.80	2.131 ± 0.255	0.115	S	–
	J181810.16-333457.2	RS27	18:18:10.17	–33:34:57.30	55.402 ± 0.539	0.132	C	–
	J181810.51-333506.5	RS28	18:18:10.51	–33:35:06.50	13.791 ± 0.715	0.132	M	–
J1819.9-2926	J182013.01-292750.5	RS29	18:20:13.02	–29:27:50.60	1.309 ± 0.205	0.109	S	–
	J182008.42-293010.8	RS30	18:20:08.72	–29:30:13.10	2.89 ± 0.324	0.111	S	–
	J182008.71-293013.0	RS31	18:20:08.43	–29:30:10.80	7.107 ± 0.96	0.111	S	–
J1820.7-3217	J182045.41-321609.6	RS32	18:20:45.41	–32:16:09.70	2.285 ± 0.238	0.116	S	–
J1828.2-3252	J182817.08-325520.5	RS33	18:28:17.08	–32:55:20.50	11.129 ± 0.943	0.120	M	–
	J182811.38-325651.9	RS34	18:28:11.39	–32:56:51.94	1.383 ± 0.270	0.118	S	–

Notes. The columns, from left to right, are: ID of UGS from 4FGL catalog; ID of RS from VLASS catalog; number identification for RS; right ascension (J2000) for RS; declination (J2000) for RS; $F_{\rm tot}$ is the integrated flux density of the component in the S-band; σ_S is uncertainty in total flux; $S_{\rm code}$ is a component type of Gaussian fitting: S (single Gaussian fit), C (single Gaussian fit in an island with other components), or M (multi Gaussian fit); additional classification of the VLASS source. The acronyms for additional classifications are: PN (planetary nebula), YSO (young stellar object), and AGN (active galactic nuclei). [(a)]Frew et al. (2013), [(b)]Jacoby et al. (2021), [(c)]Kuhn et al. (2021), [(d)]Schmidt et al. (2025), [(e)]Donoso et al. (2024).

employed a triple-criterion approach using complementary statistical estimators: the fractional variability amplitude ($F_{\rm var}$), the reduced chi-squared ($\chi^2_{\rm red}$), and the Kolmogorov-Smirnov (K–S) test.

The fractional variability amplitude was calculated following the prescription of Vaughan et al. (2003):

$$F_{\rm var} = \sqrt{\frac{S^2 - \langle\sigma^2_{\rm err}\rangle}{\langle x\rangle^2}}, \quad (1)$$

where S^2 is the total variance, $\langle\sigma^2_{err}\rangle$ is the mean square of the measurement uncertainties, and $\langle x\rangle$ is the mean magnitude.

While $F_{\rm var}$ provides a direct measure of the physical magnitude of the fluctuations, we used $\chi^2_{\rm red}$ and the K–S test to establish statistical significance from different perspectives. The reduced chi-squared ($\chi^2_{\rm red} = \chi^2/{\rm d.o.f.}$, where d.o.f. is the degrees of freedom) evaluates the overall goodness of fit against a constant model and is sensitive to total data dispersion. In parallel, the K-S test assesses the probability (p value) of the observed magnitude distribution deviating from a normal distribution expected from purely stochastic noise.

To ensure the reliability of our detections against instrumental systematics and the intrinsic stochastic nature of astronomical sources, we performed a significance test based on red noise simulations. We modeled the background fluctuations using a damped random walk (DRW) process, which is characterized by a power spectral density of $P(f) \propto f^{-2}$ at high frequencies. This model offers a more accurate depiction of astrophysical variability compared to white-noise models.

Implementing the DRW model and subsequent significance thresholds required refined data quality control. Consequently, the final number of points (N_{pts}) for each source was adjusted to ensure reliable temporal sampling. This process involved removing outliers and observations whose uncertainties significantly

Table 2. List of five NIR sources that could be extragalactic sources associated with UGS.

4FGL	ID	Z	Y	J	H	K_s	VVV ID	Sep.
J1745.6-3626	RS17	19.140 ± 0.265	18.606 ± 0.234	18.091 ± 0.224	17.351 ± 0.205	16.793 ± 0.134	VVV-J174555.13-362331.2	1.02″
J1814.7-3420	RS23	19.158 ± 0.134	18.768 ± 0.134	17.984 ± 0.071	17.174 ± 0.076	16.400 ± 0.034	VVV-J181446.75-342341.3	0.63″
J1816.4-2727	RS24	17.795 ± 0.083	17.320 ± 0.075	16.532 ± 0.050	15.747 ± 0.045	15.160 ± 0.032	VVV-J181628.80-272603.1	0.36″
J1817.2-3035	RS25	18.198 ± 0.099	17.730 ± 0.083	17.040 ± 0.058	16.232 ± 0.050	15.515 ± 0.031	VVV-J181720.40-303300.0	0.44″
J1828.2-3252	RS33	16.575 ± 0.010	16.166 ± 0.011	15.501 ± 0.007	14.756 ± 0.008	14.274 ± 0.005	VVV-J182817.04-325521.0	0.92″

Notes. The columns, from left to right, are: ID of UGS from 4FGL catalog; number identification for RS; the means of the Z, Y, J, H and K_s magnitudes; VVV identifications of NIR; separation between NIR and RS (expressed in arcsec).

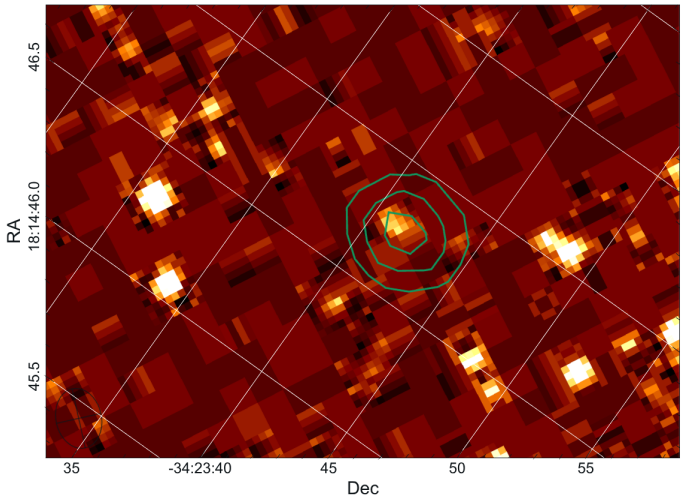

Fig. 3. VVV image in K_s band of RS23 (UGS J1814.7-3420). Green lines show the contour levels of the VLASS J181446.75-342340.7 source.

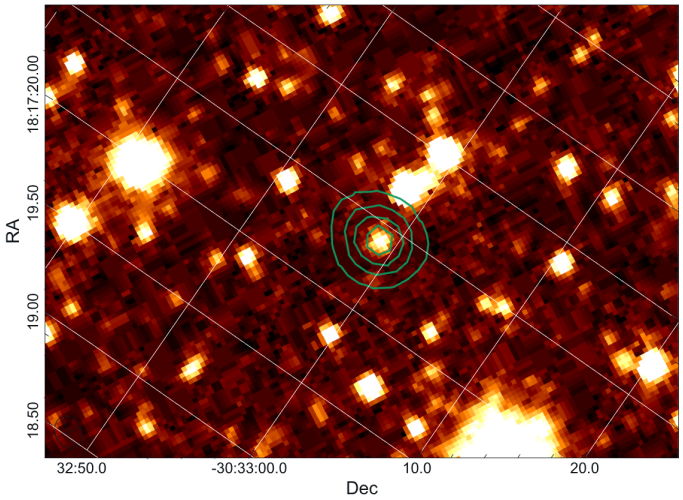

Fig. 5. VVV image in K_s band of RS25 (UGS J1817.2-3035). Green lines show the contour levels of the VLASS J181720.39-303258.5 source.

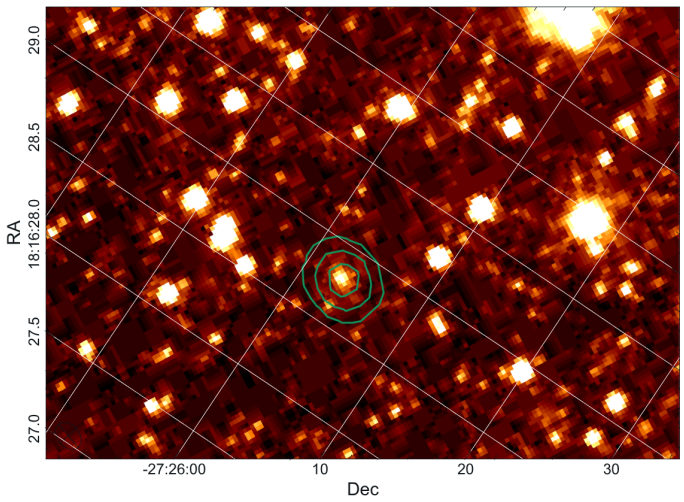

Fig. 4. VVV image in K_s band of RS24 (UGS J1816.4-2727). Green lines show the contour levels of the VLASS J181628.79-272602.8 source.

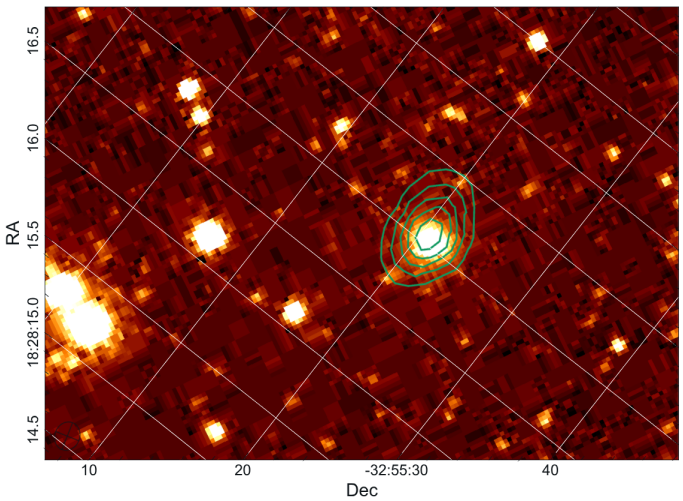

Fig. 6. VVV image in K_s band of RS33 (UGS J1828.2-3252). Green lines show the contour levels of the VLASS J182817.08-325520.5 source.

exceeded the sample mean. This ensured that the variability analysis would not be affected by poor-quality data or uncorrelated noise.

For each source, we generated 10 000 synthetic light curves that replicate the exact observational cadence (MJD) and the mean measurement uncertainties of the real data. These simulations allowed us to determine a conservative confidence threshold; that is, a source is considered genuinely variable only if its observed $F_{\rm var}$ and $\chi^2_{\rm red}$ exceed 99% of the distribution generated by these red-noise trajectories.

The results for the five analyzed sources are summarized in Table 3. Furthermore, we ran a Stetson algorithm (Stetson 1996) and identified all of them as potential variable sources ($J_S > 0.5$).

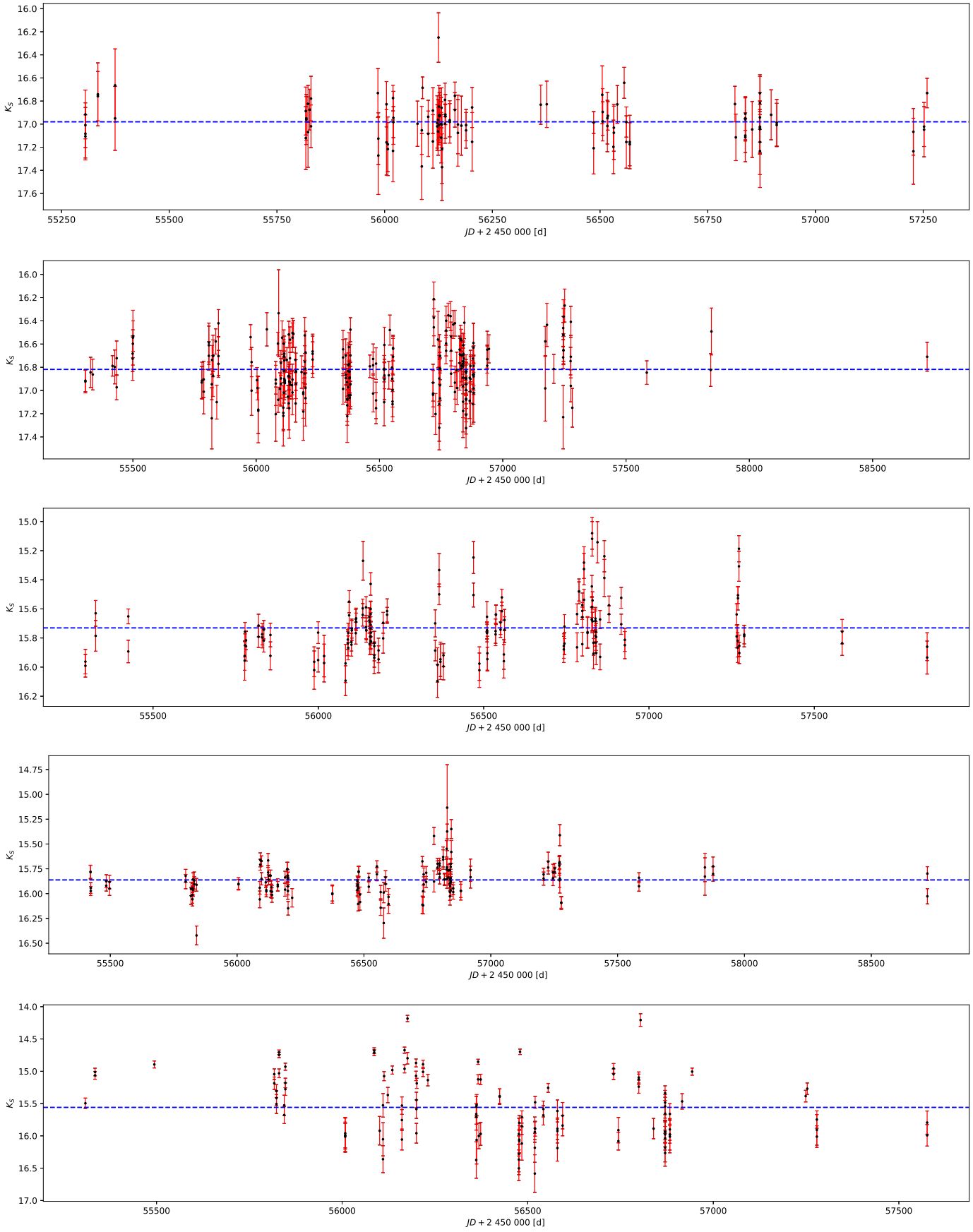

Fig. 7. K_s-band light-curves for five blazar candidates. The graphics correspond from top to bottom to RS17 (J1745.6-3626), RS23 (J1814.7-3420), RS24 (J1816.4-2727), RS25 (J1817.2-3035), and RS33 (J1828.2-3252). The error bars are shown in red, and the mean value is represented by the blue dashed line.

Table 3. Summary of variability analysis.

ID	N_{pts}	$\chi^2_{\rm red}$	F_{var} (%)	K-S p-value	Classification
RS17	135	1.18	1.32	0.041	Marginal candidate
RS23	110	1.05	0.95	0.152	Non-variable
RS24	128	1.42	2.15	0.002	Variable
RS25	115	0.98	<0.5	0.420	Non-variable
RS33	142	1.59	3.41	0.0001	Confirmed variable

Notes. The columns, from left to right, are: ID of the RS corresponding to the VVV source; number of data points after the cleaning procedure ($\sigma_{err} < 0.25$); reduced chi-squared (χ^2/d.o.f.), where a value significantly greater than 1 indicates a departure from the constant model; fractional variability amplitude, representing the percentage of intrinsic flux variation after subtracting instrumental noise; p-value from the Kolmogorov-Smirnov test, values lower than 0.05 indicate that the magnitude distribution is statistically inconsistent with a constant source; final classification based on the triple-criterion consensus.

3.3. Radio data

We used radio observations from the Rapid ASKAP Continuum Survey (RACS, McConnell et al. 2020), conducted with the Australian Square Kilometre Array Pathfinder (ASKAP) telescope, in the 700–1800 MHz frequency range. The RACS survey covered the entire sky visible from the ASKAP site in the southern hemisphere, with declinations ranging from −90° to +51°. We created cutouts[2] around the coordinates of five blazar candidates using image data sets from three RACS bands (Duchesne et al. 2025): 887.5 MHz with a bandwidth of 288 MHz (RACS-low), 1295.5 MHz with a bandwidth of 144 MHz (RACS-mid), and 1655.5 MHz with a bandwidth of 288 MHz (RACS-high). RACS can reach sensitivities of 0.25 mJy/beam with resolutions of 25″ (RACS-low), and 0.2 mJy/beam with resolutions of ∼9.5″ (RACS-mid and -high).

We fit a 2D gaussian profile (Condon 1997) to estimate the total flux density for each band and created SED profiles for these bands (Fig. 8). To compare the profiles, in Fig. 9 we show the normalized fluxes. The SED modeling does not account for intrinsic variability. RACS-low was conducted in separate campaigns from April 2019 to mid-2020, and RACS-mid was conducted in a later epoch. We emphasize that different epochs can affect the interpretation of blazar spectra. However, the SEDs of four blazar candidates show a secondary low-frequency turnup $\nu_{\rm trough-rest}$ higher than the mean value of 1 GHz found by Behiri et al. (2025) in the characterization of the blazar SEDs.

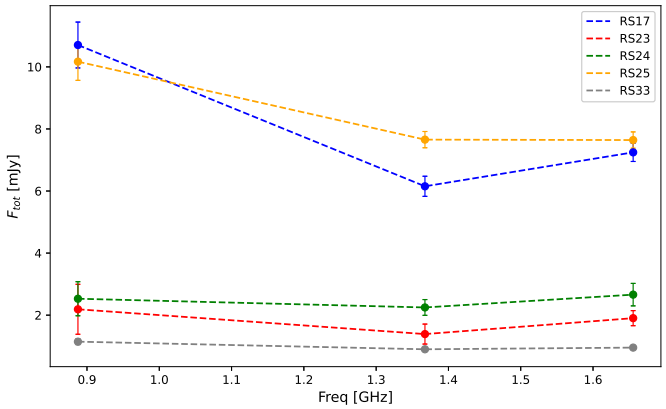

Fig. 8. Spectral energy distributions for five blazar candidates (RS) shown at 887.5 MHz (RACS-low), 1295.5 MHz (RACS-mid), and 1655.5 MHz (RACS-high), with error bars.

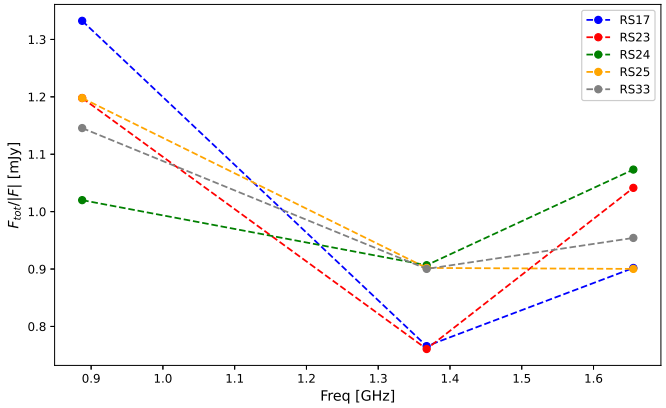

Fig. 9. Spectral energy distributions with normalized fluxes for five blazar candidates (RS) shown at 887.5 MHz (RACS-low), 1295.5 MHz (RACS-mid), and 1655.5 MHz (RACS-high).

4. Results

UGS J1745.6-3626 contains three sources within the 95% confidence *Fermi* error ellipse. Two of these sources, RS15 and RS16, are separated by about 10″. One of them was reported as a multi-Gaussian fit in the VLASS catalog. Recently, Stein et al. (2021) modeled an SED and obtained a spectral index of $\alpha = -0.95$ at frequencies of 150 MHz, 842 MHz, and 1.4 GHz using observations from the TIFR GMRT Sky Survey Alternative Data Release (TGSS ADR, Intema et al. 2017), the Molonglo Galactic Plane Survey (MGPS, Murphy et al. 2007), and the NRAO VLA Sky Survey (NVSS, Condon et al. 1998), respectively. We also applied our CMDs and CCD analysis to the NIR source near to RS15 and RS16, but the results were negative. The third source, RS17, has an NIR source at 1.02″ that meets the CCD and variability criteria for a blazar candidate (Fig. A.1). Nevertheless, RS17 was classified as a marginal candidate under the stringent criteria imposed by the red-noise simulations. Although it shows slight deviations from a constant model, its fluctuation amplitude is consistent with the tail of the simulated red noise distribution. Therefore, we adopted a conservative interpretation, acknowledging that a combination of low-level intrinsic activity and residual instrumental effects could explain the observed behavior.

UGS J1814.7-3420 only contains the radio source VLASS1QLCIR J181446.75-342340.7 (RS23), which lies within the 95% confidence *Fermi* error ellipse. RS23 has an integrated flux of 1.562 ± 0.209 mJy at the *S* band. This radio source has a nearby NIR source located in the CCD region labeled B (Fig. A.2), which is separated by 0.63″. This NIR source exhibits relative stability in red-noise simulations, with variations primarily driven by measurement noise.

UGS J1816.4-2727 has a radio source, VLASS1QLCIR J181628.79-272602.8 (RS24), for which Schinzel et al. (2017) follow-up observations were performed using the Australia

[2] The RACS cutouts were obtained from the public domain https://data.csiro.au/.

Telescope Compact Array (ATCA) and the JVLA within the 4 − 10 GHz range. They determined the flux density at two frequencies with a 2 GHz bandwidth: 4.2 ± 0.2 mJy at 5.5 GHz and 4.5 ± 0.4 mJy at 9 GHz. This resulted in a spectral index of $\alpha = 0.14$. Bruzewski et al. (2021) used dedicated VLA observations at the *C*-band receiver (4−8 GHz) and combined them with data from the VLASS catalog at the *S* band. They obtained integrated fluxes of 3.250 ± 0.225 mJy (3 GHz), 2.100 ± 0.0992 mJy (5 GHz), and 3.820 ± 0.2060 mJy (7 GHz), as well as a spectral index of $\alpha = 0.261 \pm 0.120$ using the integrated flux values at three frequencies. There are two NIR sources near RS24, but the closer one (0.36″) is near the edge of the CCD region labeled B (Fig. A.3). This NIR source meets the color-color criteria of Baravalle et al. (2023) and was identified as variable using red-noise simulations. This object is a high-priority candidate for follow-up observations to characterize its physical nature due to the combination of high fractional variability and a low *p* value.

For UGS J1817.2-3035, Donoso et al. (2024) found four NIR sources, two of which are located in the A region and two in the B region of the CCD (Fig. A.4). They proposed a VVV object (coordinates RA = 18 : 17 : 20.41 and Dec = −30 : 32 : 58.90) as an early-type galaxy candidate for the UGS counterpart. We only found a radio source, VLASS1QLCIR J181720.39-303258.5 (RS25), with an integrated flux of 5.802 ± 0.221 mJy at the *S* band. Schinzel et al. (2017) determined integrated fluxes 6.0 ± 0.2 mJy at 5.5 GHz and 5.7 ± 0.2 mJy at 9 GHz, resulting in a spectral index of $\alpha = -0.1$. The RS25 is located at a distance of 0.44″ from the proposed NIR source by Donoso et al. (2024). Its fractional variability amplitude ($F_{\rm var}$) is less than 0.5, and its magnitude distribution is statistically consistent with a constant model (K-S $p-$value > 0.3). Additionally, RS25 is relatively stable in red-noise simulations, with variations primarily attributed to measurement noise.

For UGS J1828.2-3252, there are two radio sources within the 95% confidence *Fermi* error ellipse. The VLASS catalog duplicated detections from each source. Two different flux values have been measured for RS33 at 3 GHz: 11.129 ± 0.943 mJy (multi-Gaussian fit, Duplicate_flag = 1) and 7.862 ± 0.519 mJy (single-Gaussian fit, Duplicate_flag = 2). Bruzewski et al. (2021) observed this source with the VLA in the *C* band and obtained integrated fluxes of 2.860 ± 0.119 mJy at 5 GHz and 3.130 ± 0.225 mJy at 7 GHz. However, they considered the the target with a single-Gaussian fit (VLASS1QLCIR J182817.06-325520.5) and flux of 7.862 ± 0.519 mJy at 3 GHz to estimate a spectral index of $\alpha = -1.552 \pm 0.403$. We chose the target with a multi-Gaussian fit, VLASS1QLCIR J182817.08-325520.5 and higher flux. The RS33 NIR source, located at 0.36″, meets the CCD criteria (Fig. A.5) and exhibits the strongest evidence of intrinsic variability. It has a high $\chi^2_{\rm red}$ of 1.59, a significant fractional amplitude of 3.41%, and a K-S *p* value of 0.0001, which is inconsistent with stochastic fluctuations ($p < 0.01$). In this specific case, the sample size was optimized to 142 points by including high-cadence intraday observations. This increased density is essential for accurately determining the damping timescale (τ) using the DRW model. It also ensures that the higher $F_{\rm var}$ observed is not due to sparse sampling. Using the JHK_s-bands of VVV and the optical images from the DECam Plane Survey (DECaPS2, Saydjari et al. 2022), we found visual evidence of a diffuse object, consistent with the presence of an elliptical galaxy.

5. Conclusions

From an initial sample of 318 UGSs, we selected 22 targets that had at least one detected continuum radio source in the *S* band of the VLASS catalog and were located within the 95% confidence *Fermi* error ellipse. The 22 targets had a total of 34 RSs. Only five RSs were associated with an NIR source from the VVV survey that meets the CMD and CCD criteria and shows variability. We propose the following four NIR sources as blazar candidates for the UGSs: J1745.6-3626, J1814.7-3420, J1816.4-2727, and J1817.2-3035. We found evidence indicating that J1828.2-3252 is consistent with an elliptical galaxy undergoing a merging process.

In Table 1, RS01 and RS08 are shown, which were previously classified as planetary nebulae. We did not find evidence of an extragalactic source for these objects in the CMD and CCD analyses, even though the central star of a planetary nebula can be detected in the NIR (see Minniti et al. 2025). To determine the origin of these UGSs (J1714.9-3324 and J1737.2-2808, respectively), more observations are needed.

We achieved a robust characterization of the five sources in our sample through statistical analysis of variability, which was reinforced by red-noise simulations. Using a multi-method approach, we confirmed that UGS J1816.4-2727 and UGS J1828.2-3252 exhibit significant intrinsic variability. The most robust results were found in UGS J1828.2-3252, where all statistical criteria were met: a high $\chi^2_{\rm red}$ (1.59), a significant fractional amplitude (3.41%), and a K–S *p* value (0.0001) well below the significance threshold. This consistency provided high confidence in the astrophysical nature of the detected fluctuations for these two sources. Regarding the sources with lower variability amplitudes, such as UGS J1745.6-3626, we took a more cautious approach to interpretation. Although this source exhibits slight deviations from stability, our DRW simulations suggest that these fluctuations are not sufficiently decoupled from the expected stochastic background. We emphasize that, in the regime of $F_{\rm var} \lesssim 1.5\%$, the potential impact of residual instrumental systematics and correlated noise becomes non-negligible. While these objects are still of interest, their classification as genuinely variable is currently limited by the available photometric sampling. Further high-cadence monitoring and improved sensitivity are therefore essential for definitively distinguishing low-level, intrinsic astrophysical signals from complex instrumental noise.

Particularly, the blazar candidates for UGS J1745.6-3626, 1814.7-3420, 1816.4-2727, and J1828.2-3252 exhibit a peaked SED with a secondary low-frequency turn-up $\nu_{\rm trough-rest}$ between 0.9 and 1.3 GHz. This can be explained by the fact that the spectrum of the central region dominates the broad, pronounced component on a kiloparsec scale (see Edwards & Tingay 2004). This results in an overall spectrum that rises at low frequencies. The blazar candidate for UGS J1817.2-3035 (RS26) does not exhibit a low-frequency turn-up in the RACS wavelength range. However, it can be described by a simple power-law model, $S_\nu \propto \nu^{-0.1}$, by using the spectral index determined in Schinzel et al. (2017). Future work dedicated to observing these five blazar candidates at radio continuum frequencies higher than 1.6 GHz will help determine their turnover peak frequencies, ν_p, which are evidence of synchrotron self-absorption. The spectral index ratio of the optically thin and thick components, $\alpha_{\rm thick}$ ($\nu < \nu_p$) and $\alpha_{\rm thin}$ ($\nu > \nu_p$), respectively, could be used as a proxy for the blazar population of FSRQs and BL Lacs.

Acknowledgements. This paper was partially supported by the National Scientific and Technical Research Council (CONICET), as well as by the CICITCA

grant (code 80020220100090SJ) for the period 2023–2024. This work has made used of data from the fourth Fermi Large Area Telescope Data Release 3, the Very Large Array Sky Survey, the VISTA Variables in the Via Lactea Survey, and the Rapid ASKAP Continuum Survey. R.K.S. acknowledges support from CNPq/Brazil through projects 308298/2022-5 and 421034/2023-8. D.M. acknowledges support by ANID Fondecyt Regular grant No. 1220724, and by the BASAL Center for Astrophysics and Associated Tecnologies (CATA) through ANID grant FB210003.

References

Acero, F., Donato, D., Ojha, R., et al. 2013, ApJ, 779, 133
Ackermann, M., Ajello, M., Allafort, A., Antolini, E., & Baldini, L. 2012, ApJ, 753, 83
Ajello, M., Angioni, R., Axelsson, M.et al. 2020, ApJ, 892, 105
Atwood, W. B., Abdo, A. A., Ackermann, M., et al. 2009, ApJ, 697, 1071
Ballet, J., et al. (The Fermi-LAT collaboration) 2023, ArXiv e-prints [arXiv:2307.12546]
Baravalle, L. D., Schmidt, E. O., Alonso, M. V., et al. 2023, MNRAS, 520, 5950
Behiri, M., Mahony, E. K., Sadler, E., et al. 2025, A&A, 702, A10
Blandford, R. D., & Königl, A. 1979, ApJ, 232, 34
Bruzewski, S., Schinzel, F. K., Taylor, G. B., & Petrov, L. 2021, ApJ, 914, 42
Catelan, M., Minniti, D., Lucas, P. W., et al. 2011, in RR Lyrae Stars, Metal-Poor Stars, and the Galaxy, ed. A. McWilliam, 5, 145
Cavaliere, A., & D'Elia, V. 2002, ApJ, 571, 226
Chen, Z., Gu, M., & Cao, X. 2009, MNRAS, 397, 1713
Cioni, M.-R., Clementini, G., Girardi, L., Guandalini, R., & Gullieuszik, M. 2011, The Messenger, 144, 25
Cioni, M.-R. L., Kamath, D., Rubele, S., et al. 2013, A&A, 549, A29
Condon, J. J. 1997, PASP, 109, 166
Condon, J. J., Cotton, W. D., Greisen, E. W., et al. 1998, AJ, 115, 1693
D'Abrusco, R., Álvarez Crespo, N., Massaro, F., et al. 2019, ApJS, 242, 4
Donoso, L. G., Pichel, A., Baravalle, L. D., et al. 2024, MNRAS, 529, 1019
Duchesne, S., Ross, K., Thomson, A. J. M., et al. 2025, PASA, 42, 38
Edwards, P. G., & Tingay, S. J. 2004, A&A, 424, 91
Fossati, G., Maraschi, L., Celotti, A., Comastri, A., & Ghisellini, G. 1998, MNRAS, 299, 433
Frew, D. J., Bojičić, I. S., & Parker, Q. A. 2013, MNRAS, 431, 2
Gordon, Y. A., Boyce, M. M., O'Dea, C. P., et al. 2021, ApJS, 255, 30
Intema, H. T., Jagannathan, P., Mooley, K. P., & Frail, D. A. 2017, A&A, 598, A78
Jacoby, G. H., Hillwig, T. C., Jones, D., et al. 2021, MNRAS, 506, 5223
Kuhn, M. A., de Souza, R. S., Krone-Martins, A., et al. 2021, ApJS, 254, 33
Lefaucheur, J., & Pita, S. 2017, A&A, 602, A86
Lister, M. L., Homan, D. C., Hovatta, T., & Kellermann, K. I. 2019, ApJ, 874, 43
Marchesini, E. J., Paggi, A., Massaro, F., et al. 2019, A&A, 631, A150
Marchesini, E. J., Reynaldi, V., Vieyro, F., et al. 2023, A&A, 670, A91
Massardi, M., Bonaldi, A., Bonavera, L., et al. 2016, MNRAS, 455, 3249
Massaro, E., Maselli, A., Leto, C., et al. 2015, Ap&SS, 357, 75
Massaro, F., D'Abrusco, R., Ajello, M., Grindlay, J. E., & Smith, H. A. 2011, ApJ, 740, L48
Massaro, F., D'Abrusco, R., Giroletti, M., et al. 2013, ApJS, 207, 4
Massaro, F., D'Abrusco, R., Tosti, G., et al. 2012a, ApJ, 750, 138
Massaro, F., D'Abrusco, R., Tosti, G., et al. 2012b, ApJ, 752, 61
McConnell, D., Hale, C. L., Lenc, E., et al. 2020, PASA, 37, e048
Minniti, D., Fragkou, V., Alonso-García, J., Majaess, D., & Cortesi, A. 2025, A&A, 702, A79
Minniti, D., Lucas, P. W., Emerson, J. P., & Saito, R. K. 2010, New Astron., 15, 433
Mohan, N., & Rafferty, D. 2015, Astrophysics Source Code Library [record ascl:1502.007]
Murphy, T., Mauch, T., Green, A., et al. 2007, MNRAS, 382, 382
Padovani, P., Alexander, D. M., Assef, R. J., et al. 2017, A&ARv, 25, 2
Paggi, A., Massaro, F., D'Abrusco, R., et al. 2013, ApJS, 209, 9
Paiano, S., Falomo, R., Treves, A., & Scarpa, R. 2020, MNRAS, 497, 94
Peirson, A. L., Liodakis, I., & Romani, R. W. 2022, ApJ, 931, 59
Pichel, A., Donoso, L. G., Baravalle, L. D., et al. 2020, MNRAS, 491, 3448
Saito, R. K., Hempel, M., Alonso-García, J., et al. 2024, A&A, 689, A148
Saydjari, A., Schlafly, E., Lang, D., et al. 2022, Am. Astron. Soc. Meet. Abstr., 240, 318.06
Schinzel, F. K., Petrov, L., Taylor, G. B., & Edwards, P. G. 2017, ApJ, 838, 139
Schlafly, E. F., & Finkbeiner, D. P. 2011, ApJ, 737, 103
Schmidt, E. O., Baravalle, L. D., Pichel, A., et al. 2025, MNRAS, 544, 152
Smith, L. C., Lucas, P. W., Koposov, S. E., et al. 2025, MNRAS, 536, 3707
Stein, Y., Vollmer, B., Boch, T., et al. 2021, A&A, 655, A17
Stetson, P. B. 1996, PASP, 108, 851
Stickel, M., Padovani, P., Urry, C. M., Fried, J. W., & Kuehr, H. 1991, ApJ, 374, 431
Urry, C. M., & Padovani, P. 1995, PASP, 107, 803
Vaughan, S., Edelson, R., Warwick, R. S., & Uttley, P. 2003, MNRAS, 345, 1271
Wright, E. L., Eisenhardt, P. R. M., Mainzer, A. K., & Ressler, M. E. 2010, AJ, 140, 1868
Yang, J. H., Fan, J. H., Liu, Y., et al. 2022, ApJS, 262, 18

Appendix A: CMD and CCD

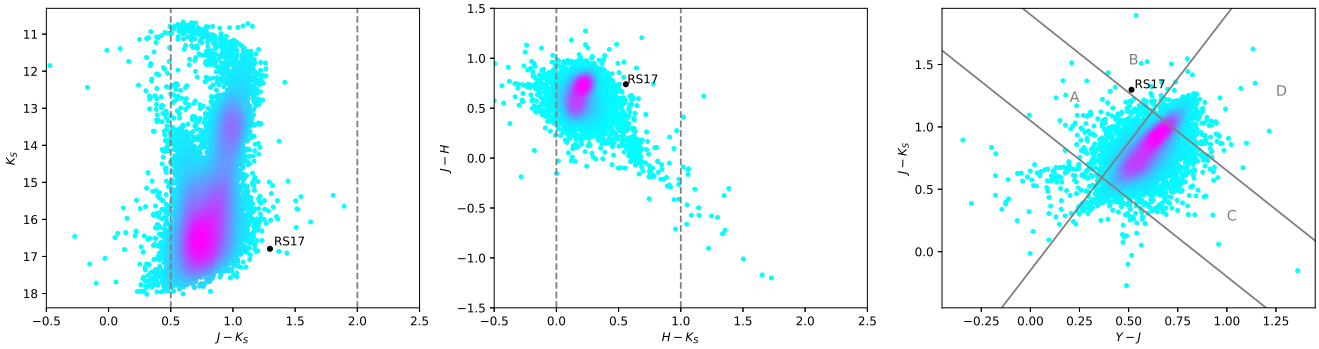

Fig. A.1. Color-magnitude diagrams (CMDs) and color-color diagram (CCD) of the $YJHK_S$ passbands for blazar candidates. The source VVV-J174555.13-362331.2 (RS17) is marked with a black circle. The magenta-cyan color map corresponds to the density of VVV objects lying within the positional uncertainty region of the UGS. In the CMDs, the dashed gray lines correspond to the color criteria of Baravalle et al. (2023). For the CCD, the solid gray lines and labeled regions are defined by Cioni et al. (2013).

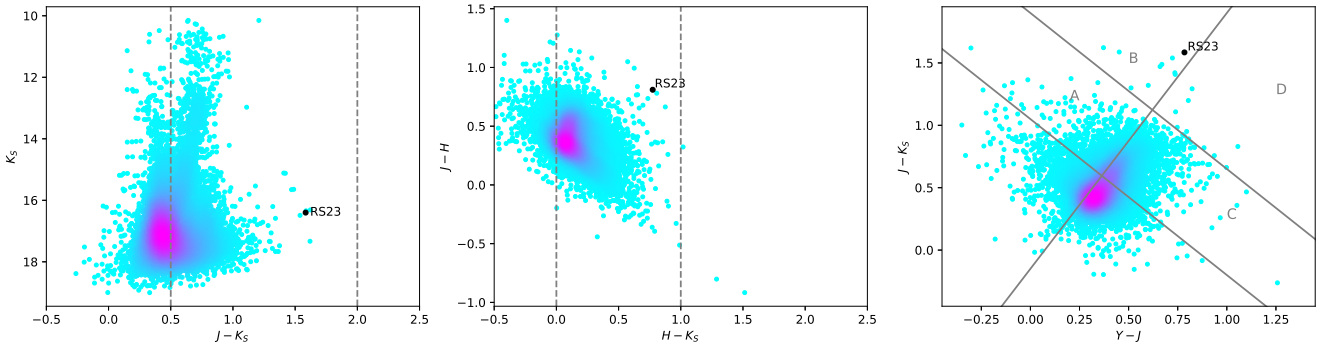

Fig. A.2. CMD and CCDs of the $YJHK_S$ passbands for the source VVV-J181446.75-342341.3 (RS23).

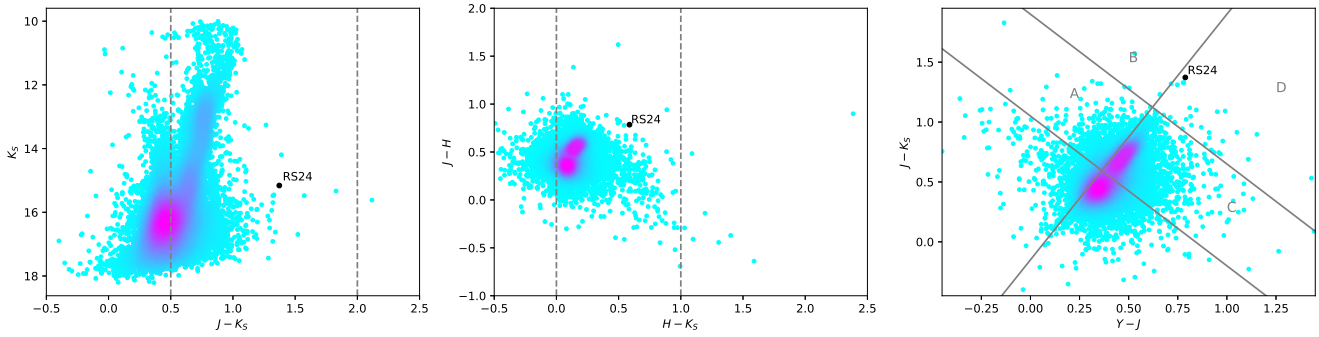

Fig. A.3. CMD and CCDs of the $YJHK_S$ passbands for the source VVV-J181628.80-272603.1 (RS24).

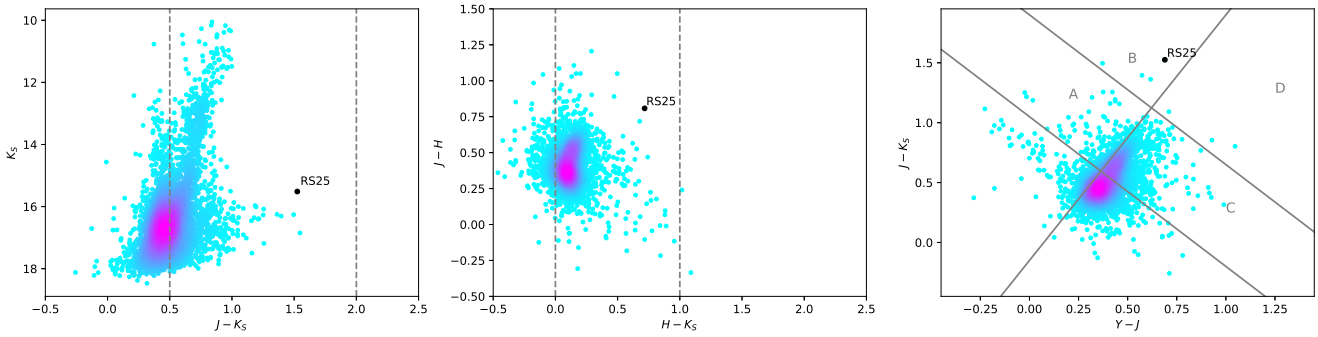

Fig. A.4. CMD and CCDs of the $YJHK_S$ passbands for the source VVV-J181720.40-303300.0 (RS25).

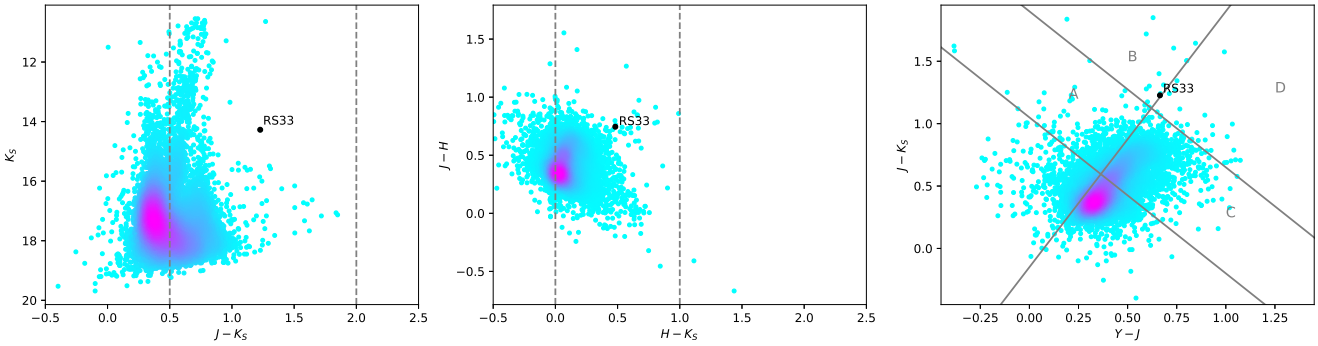

Fig. A.5. CMD and CCDs of the $YJHK_S$ passbands for the source VVV-J182817.04-325521.0 (RS33).